

Nanoscale Non-Contact Laser Measurement of Precision Machine Tooling and Optical Surfaces

Schubert Soares

Ultrafast Sensors, 6774 E 123rd Ave, Brighton, CO 80602, U.S.A.

Keywords: Non-Contact Nano Metrology, Laser Triangulation, Optical Scatter, Machine Tool Error, Surface Topography, Edge Structure, Defect Geometry, Thin Films.

Abstract: Optical and semiconductor products are fabricated utilizing industrial technology that is steadily progressing to nanometre accurate operations. Reliable non-invasive contact-free sensors and techniques are required to monitor *in situ* manufacturing parameters in parallel with product formation. The real-time evaluation and analysis of precision fabrication processes could lead to intelligent, computerized, sensor-actuated implementation, with automated compensating feedback loops to facilitate nanometre accuracy and consistently provide high quality products in abundant yield. Laser triangulation is demonstrated herewith as a versatile solution to simultaneously measure machine tool components and monitor the product in process. Optically levered reflection resolved on a nanometre resolution displacement sensor, enables the analysis of spindle axial and rotational error, stage linear error, the impact of these error-motion components on a diamond tool edge and its progression to wear, while inspecting the compliance of the product to the desired surface finish and shape. Scanning optical scatterometry is utilized to image and analyse edges, surfaces, defects, and thin film structure. This sensor technology is highly adaptable, and may be utilized in scales ranging from small μm -size to large meter-size products manufactured from a variety of materials.

1 INTRODUCTION

A variety of industrial and consumer products such as laser optics, mirrors, crystals, thin films, fibre optic devices, camera optics, semiconductor wafers, precision aircraft and automotive engine components, and progressive-focus optical lenses are routinely manufactured to accuracies, ranging from a few 100's to a few nanometres. The manufacture of these products is implemented with rigid process control, often utilizing separate systems for metrology, in uncoordinated independent procedures. There is vital requirement in these diverse industries for versatile, integrable, contact-free, non-destructive, optical sensor technology to accurately monitor *in situ* all dynamics of the fabrication process, machine tool operating parameters, cutting tools, and product quality. The measurements range from rotational (spindle) and linear (stage) error motion, cutter condition *vis-à-vis* edge quality and evolution during usage, machined surface quality and shape conformity, defects, and manufacturing repeatability. The potential for co-ordinated

concurrent sensor measurements and computer assisted parametric control of the manufacturing process could result in consistent nanometre quality products with significantly improved yield.

Conventional contact-free techniques such as capacitive and inductive probes rely on relatively large sampling areas, and may be inadequate in terms of convenience, calibration, sensitivity, and cost for a variety of product materials, shapes, and sizes. These systems were developed originally for conductive materials; the non-invasive measurement of optics or doped semiconductors poses additional challenges. Shape is another restriction with calibration posing significant hurdles for spherical, aspheric, or free form surfaces, restricting usage to planar products. Other techniques such as ultrasonics, air pressure, and phase analysis involve greater hardware complexity and lack nanometre-level resolution. The measurement of the shape of a diamond cutting tool, or the structure of a thin film, or a defect for example, is virtually impossible utilizing any of these technologies. Since all of these sensor types require extensive electronic

processing and amplification, noise and linearity are major limiting factors to accuracy and resolution.

Laser triangulation sensing offers a simple, compact, feasible, micro-to-macro scale solution to track operating parameters in a variety of industrial environments, to monitor, evaluate, and analyse the manufacturing process, and also to measure a multitude of precision products fabricated from a variety of materials. Optical-lever metrology, in which laser reflection and scatter are scanned on a nanometre-resolution solid state sensor, is investigated in this paper. This technology is utilized to easily resolve 100-nm tool displacement, 250-nm error motion, cutting tool shape and wear, machined surface quality and tolerances, defects, and composite thin films. The versatility of this technology resides in simple calibration processes, easy multi-channel expansion into ordinary data acquisition and computer systems, and turnkey integration with precision machine tools.

2 OPTICAL METROLOGY

There are several well established techniques for optical metrology utilizing the energy (wavelength), the coherence, and the polarization properties of laser beams, in electromagnetic interaction with surfaces and media, derived from the physics of optical reflection, diffraction, or transmission. The optical signals are monitored with sensors or cameras, recorded on data acquisition systems, and analysed and decoded with software to produce calibrated metrics for evaluation and quality control.

The foremost of these methods is interferometry wherein a pair of coherent beams, originating from the same source (via wavefront or amplitude division, forming reference and probe beams) interact when combined after sampling to produce fringe energy redistributions, which are monitored singly, sequentially, or collectively to decode a variety of parameters. The signal could be related to and utilized to measure, for example, displacement, three-dimensional (3D) shape, spectral content, optical properties, and the internal structure of optically transmissive media. The reflection and transmission properties of polarized light incident on near-perfect surfaces, interfaces, and film layers provides additional opportunities for metrology based on ellipsometry, Brewsters angle, principal angle, critical angle and total internal reflection (Azzam, 1999, Heavens, 1955). These techniques in fact may be utilized, by comparative analysis of polarization state, amplitude evanescence, and phase

shift, to measure real and complex optical properties of media, examine sub-surface structure, or detect anomalous behaviour at interfaces.

Optical triangulation and scatter, operating with nanopositioning, are additional options available to directly evaluate position, displacement, and motion, and to image surface topography, sub-surface structure, anisotropies, artefacts, defects, and thin films.

2.1 Laser Reflection and Scatter

Our primary focus is on laser reflection and scatter from smooth surfaces in optical components, precision-machined surfaces, Si wafers and similar products from various high-technology industries. Any smooth surface with residual nanoroughness (Figure 1) will produce specular reflection and non-specular diffractive scatter from an incident optical beam, which is preferably made diffuse to eliminate its coherence and minimize speckle. The specular beam is produced by the flat-smooth surface (zero-order roughness), and is governed by the vector Fresnel relations, which are polarization specific.

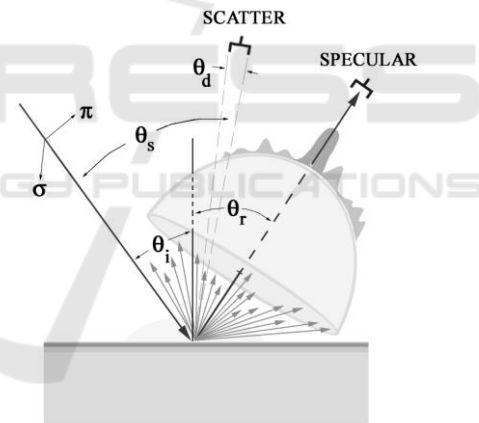


Figure 1: Geometry of optical scatterometry. Specular reflection is from the smooth surface. Low to high spatial frequency microstructure scatters proportionally decreasing power at wide angles. The omni directional low-intensity haze is produced by microstructure.

Residual structure in the surface, corresponding solely to the roughness component of the topography, can be modelled in a multi-dimensional Fourier integral (or alternate) analysis, as composed of sinusoidal (or basis) functions within a continuous and distributed spread of spatial frequencies (or components), each with adjustable amplitude and phase shift, which converges approximately, in the mean-square, to the surface profile (Church, 1979, Longuet-Higgins, 1957, Stover, 1995).

The far-field (Fraunhofer) distribution of scattered optical power from this surface at angle θ_s , from an incident beam inclined at θ_i , measured on a detector subtending solid angle θ_d , ranges from its maximum at the angle of specular reflection θ_r , decreases gradually but not necessarily uniformly or symmetrically, in $\sim 2\pi$ -steradians oriented (for detection) in spherical coordinates about the axis of the reflected beam, centred at the point of reflection (Figure 1). Since for practicality, θ_i is usually not normal, the spot on the surface is not circular, and must be accounted for if illuminated structure or defects are large in comparison. The scatter power measurement at non-normal angles is compensated by a factor of $(\cos\theta_s)^{-1}$ to normalize the orientation of the detector to the plane of the surface. The altitudinal and azimuthal variation of the scattered optical power about the specular axis need not necessarily be regular or asymptotic, and in fact may contain additional artefacts such as multiple secondary maxima superimposed with power fluctuations, uniform haze, and other variations.

The defect size, ρ , and the roughness dimension, ρ' , scaled in comparison to the wavelength, λ determine the corresponding total 3D scatter distribution (Bohren, 1998, Stover, 1995). There are five zones of scaling, namely: $\rho^{(0)} \ll \lambda$, $\rho^{(0)} < \lambda$, $\rho^{(0)} \sim \lambda$, $\rho^{(0)} > \lambda$, and $\rho^{(0)} \gg \lambda$. These can be restricted to a few categories for precision surfaces. Scatter from low spatial-frequency roughness (several multiples of the optical wavelength; $\rho' > \lambda$) is present in angular proximity to the specular reflection. Microstructure containing higher spatial frequencies ($\rho' < \lambda$) scatters power at wider angles away from the reflected beam. The scaling determines if the optical path of scatter radiation is by direct reflection from the surface or by instances or orders of multiple reflections within the roughness, prior to impinging on the detector. The power of the scattered radiation, if $\rho < \lambda$, scales with the sixth power of the dimension of defects, and varies as λ^{-4} . The non-specular radiation at oblique angles is essentially Rayleigh scatter produced by randomly oriented sub-wavelength $\rho^{(0)} \ll \lambda$ defects, surface, and sub-surface structure, and studied extensively by Church, 1979, and Stover, 1995. Indeed, scatter produced by nanostructure, where ρ' is relatively minor (at multi-lattice constant or multi-molecular dimensions) in comparison with λ , is distributed uniformly over the entire hemisphere, much as a Lambertian source, and forms a noise-power baseline. The total power distribution function may also contain Mie scatter components from fractional to multi-wavelength dimension defects ($\rho^{(0)} \sim \lambda$), Rayleigh scatter from

sub-wavelength defects ($\rho < \lambda$), and a wide range of features which additionally may be present on the surface as texture, device patterns, debris, or damage in a sub-surface region within an optical wavelength. The remaining critical variables in defect and artefact detection are the beam incidence angle and its polarization, the scattering cross section, the spot profile and size, and the detection arrangement. π -polarized light incident on a defect generates a symmetric lobular altitudinal pattern oriented orthogonal to the field, while σ -polarized light illuminating a defect produces a uniform altitudinal scatter distribution but is azimuthally lobular, i.e. a 90-degree rotation of the π field. The beam orientation and the positioning of detectors for defect detection in the scattering plane is an empirical art critically based on the selection of the polarization of the incident beam to enhance high defect-to-background contrast. For example, the normal component of π -polarization in near normal incidence could be utilized to probe embedded defects or voids with narrow oblique detection. Similarly, σ -polarization may be useful to detect a particle on a surface, where oblique incidence is combined with wide normal detection. Additional variables to consider are the specific defect shape (usually not spherical), the defect material, whether the defect resides on a dielectric or a conducting surface, and the corresponding image charge distributions. The operating wavelength λ may be judiciously selected if the background surface, the defect material, and the scatter thus produced are reasonably well understood. The angular distribution of scatter also suggests the utilization of Fourier spatial filtering to distinguish scatter profiles of a particular roughness range, device footprint, or defect type, a technique widely in use in the semiconductor industry to identify undesirable defects on processed wafers.

Figure 2 shows representative angle-resolved optical scatter data acquired at 633 nm on a polished quartz optic, in which the logarithm of the relative scatter produced is plotted versus the detector (scatter) angle, which is varied from the incident beam towards the specular reflected beam. The data follows our discussion in the previous paragraph, and the scatter power in relation to the surface roughness spread is as indicated. The dynamic range from the specular maximum power (flat surface) to the scatter minimum power (nanoroughness) is approximately 73 dB. The specific scatter power for a defined roughness spread at a prescribed angle could be resolved by deliberately machining the corresponding structure

onto a surface to enable a calibration reference in this measurement or vice versa. The scatter produced by an ideal near-perfect smooth flat reflecting surface would consist of only two components: the specular beam which would be an almost mirror image of the incident beam, with an infinitesimal fraction of the power transferred to omnidirectional uniformly distributed Rayleigh-scatter haze produced at the crystalline level, establishing the noise threshold. A polished optic, a precision diamond turned mirror, or a polished Si wafer are considered ideal surfaces, satisfying conditions of spatial frequency ergodicity, and sampling at a single point would produce a perfectly symmetrical scatter profile, which would be representative of the entire surface.

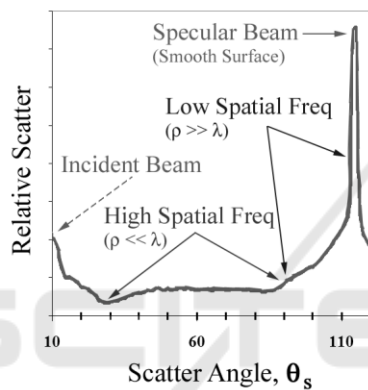


Figure 2: The angular optical scatter distribution (at $633 \text{ nm} / \pi$) measured on polished quartz. The dynamic signal range is 73 dB. The scatter power is proportional to the roughness scaled to the wavelength, as indicated.

Another useful figure of merit for comprehensive surface quality is the normalized total integrated scatter (TIS), which is produced by the entire functional structure of the surface and sub-surface, comprising all roughness and defect-array constituents with the exclusion of the specular beam (corresponding to the zero-order smooth surface), which is filtered from the data. The TIS value may be utilized to monitor a surface and provide a rapid measurement of overall quality, during the grinding, the lapping, and the polishing processes to produce a smooth flat surface on an optic or a Si wafer. It can also be utilized to sample defect density per unit area by common mode comparison of the TIS for a smooth surface to a surface with distributed defects. A surface may also be scanned in a TIS system to provide area-wide metrics for a more exact figure of merit. An associated figure of merit could be established by profiling the specular beam for

comparison with the profile of the incident beam to deduce spatial frequency components of the surface.

Precision industrial environments where optical components, devices, semiconductor wafers, and metal parts are manufactured require rapid real time evaluation and analysis of parameters such as machine error motion, surface topography, local and global surface roughness, sub-surface damage, contamination, shape, thickness, and defects. This goal is achieved if some of the technical complications, details, and analysis of scatterometry (Figure 1), associated with factors such as the angle of incidence, polarization, beam profile, interaction with media, coherence, etc., may be circumvented. A simple in-plane non-invasive linear optical system consisting of a low power plane polarized laser input beam with a symmetric profile and a passive, suitably oriented, uniaxial sensor can be devised to produce results within constraints of ease of calibration, expense budget, and low complexity. Low spatial frequency variations in surface topography or motion cause well-defined deflections in the specular reflected beam, and produce proportional signal fluctuations. If additional sensors are positioned to measure scatter in predetermined non-specular angles θ_s , it is possible to detect and deduce various surface parameters related to high spatial frequency content and defects. If the sensor is capable of resolving minute power variations, its corresponding sensitivity to surface features and defects is proportionally enhanced.

2.2 Optical Sensing

Optical sensors with wide dynamic response are available to track position, and measure displacement and motion, producing a signal, which is proportional to the relative distance between two objects, or range to a moving surface; coordinates are established by sensor geometry and mounting configuration, with illumination which can be direct beam incidence or triangulation. These sensors are available as single element units or as multi-element / dual-dimensional arrays. The sensing element could be a PIN photodiode, or a CCD or CMOS sensor, and require external bias and amplification. Optical sensing circumvents the limitations of various other non-contact technologies in measurements of planar and non-planar geometries, in a smaller footprint, with improved performance, reliability, and integration.

2.2.1 A Displacement Tracking Sensor

A planar multi-dimensional silicon sensor was demonstrated in which Schottky contact pairs were deposited and oriented laterally, with the photosensitive area delimited by the contacts as seen in the inset in Figure 3. The active area is illuminated with an optical source, preferably though not necessarily, in the profile of a collimated or focused laser beam. The optical radiation is absorbed in the sensor, inducing excitons, which instantly diffuse radially away from the point of injection, electrons dispersing more rapidly than holes, establishing a steady state charge distribution centred at the point of injection (Sze, 1981). This sensor operates on the cascading internal structure of ambipolar electrical fields, arising from the disparity in the diffusion distribution geometries of high-mobility electrons in the conduction band, and low-mobility holes in the valence band. This field arrangement modulates the intrinsic fields within the depletion region at the contacts, and induces a beam position weighted self bias at each contact, with unidirectional current flow on average that is uniquely proportional to the injection point of the optical beam relative to the contacts (Sze, 1981).

The sensor itself may be presumed to be self deconvolved and essentially noiseless, since in its passive mode internal currents, in the absence of optical input, are symmetrically opposing. If the beam profile is asymmetrical, or geometrically irregular with distributed internal power variations, then this versatile sensor could identify the weighted-average position of the “maximum” power of the beam, suggesting applications in sensing textured or patterned geometries. The sensor signal is proportional to the position of the beam maximum within the contacts, as well as to the input optical power, and also to the relative position between the plane of the active surface and the source, yielding resolvable 3D-sensitivity for a variety of applications in optical systems. The output signal may be made arbitrarily large to circumvent any level of input noise available at an amplifier; the ultimate limitation however being the shot noise in the optical source, which in effect can also be minimized by lock-in techniques, feedback control, and thermal stabilization (Horowitz and Hill, 1989).

2.2.2 Static and Dynamic Sensitivity

This sensor was evaluated for static sensitivity and dynamic response; representative results are shown in Figures 3 and 4. In the static mode a 1-mW HeNe

(633 nm) laser source was collimated into a 10X microscope objective; the beam spot was estimated at approximately 5 μm . The sensor with 150- μm active area was fixed to a micropositioning stage. The stage driver was computer controlled, and the voltage across the stage was gradually ramped, sweeping the sensor across the stationary optical beam from one contact to the opposite contact.

The functional dependence of the signal from the sensor versus the beam position traversing between the contacts is measured and processed with low noise electronics (Figure 3). This signal is shown to peak in bipolar fashion at the contacts with a null at the geometric centre. There is piecewise linearity in the signal, possibly associated with a non-uniform beam profile, shielding of the optical beam as it traverses the contact, and non-linear interaction between the ambipolar field distribution and the contact fields. Several displacement references are available for purposes of calibration; the most basic being that the manufacturer certifies the stage with a displacement per applied voltage specification. In addition, the sensor has a lateral active area dimension, which could also serve as a rigid reference.

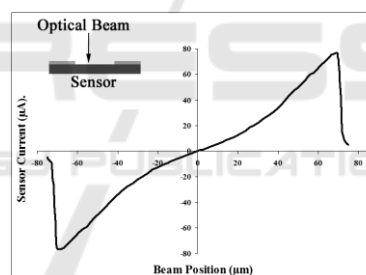


Figure 3: Tracking response of a displacement sensor.

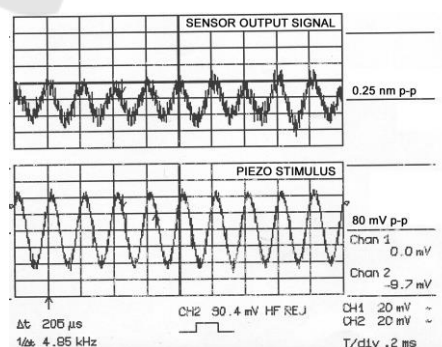


Figure 4: Frequency response of the sensor to a 4.85-kHz oscillation imposed on the optical beam.

The dynamic response of the sensor was evaluated utilizing a lock-in technique to explore low amplitude detectivity and the noise floor. The

laser was coupled into optical fibre and the fibre was fixed to a narrow tube piezoceramic with 3 nm/V displacement calibration. A 50- μm sensor was attached to a mechanical stage and positioned within the optical beam in the near field. The spot size was estimated less than 30 μm full width half maximum. The lock-in amplifier provided a 4.8-kHz, 80-mV p-p stimulus to the piezo, and the sensor signal was simultaneously monitored and measured by lock-in at 10^5 gain. The stimulus corresponds to a spatial beam oscillation of approximately 0.25 nm across the active area of the sensor, and was resolved with approximately 20% noise (Figure 4). This would indicate a detection threshold of approximately 0.05 nm, well below the lattice constant of Si. It is apparent that 1-nm resolution could routinely be achievable without any constraint.

2.3 Metrology by Laser Triangulation

The technology described above is now integrated and utilized in a computerized system to measure and evaluate a variety of manufacturing assets, operating parameters, and precision products. These range from basic tool position and displacement sensing, rotary and linear motion sensing, thermal effects, inertial imbalance, and examination of the machining operation, to sophisticated inspection of diamond cutting tools required to fabricate optics, and imaging of precision machined surfaces, defects, and thin films. The metrology and imaging system consists primarily of a stable laser source, a displacement sensor, a piezo stage with triaxial scanning capability of 50 μm x 50 μm x 50 μm , typically with 100-nm pixel resolution, ultra-low noise electronics, data acquisition, signal processing, and software analysis. The 785-nm laser is fibre coupled, and the sensor and the fibre tip are mounted adjacent, in plane on a base, with adjustments to enable the applications and measurements detailed below. The beam spot is typically under 0.1-mm diameter, and can be adjusted to the application as necessary. The optical beam and the sensor arrangement are shown in Figure 5a. This geometry of optical triangulation is optimal for sensing and imaging applications, wherein the sensor and the optical source are mutually aligned at an angle such that the source beam reflects from the target surface into the sensor, forming a plane of incidence which is orthogonal to the surface.

The displacement and motion sensitivity is as follows: if the plane of the surface moves a parallel distance δ away from its reference position (Figure 5a), the optical beam is translated to a new position

on the surface, laterally displacing the reflected beam across the sensor by a dimension, Δ , producing a proportional sensor signal. For a triangulation angle θ_i of $\pi/4$, the displacement of the beam is optically levered by a factor of twice the displacement of the surface; equivalence is established at $\sim \pi/7$. This could be considered a practical lower limit whereby the formation of a Wiener wave distribution would not perturb the sensor, in near-field measurements. The vertical response (normal to the target surface) of this configuration over a perpendicular scan of 50 μm is shown in Figure 5b. The linear response of the system in the central region is ideal for various sensing applications, which are explored in the following sections. The imaging capability of this system resides in its sensitivity to contrast in scatter measurements, in a lateral scanning process. Scatter is measured by positioning a sensor apart from the specular beam, and adjusting its altitudinal and azimuthal positions to detect spatial roughness or defect types, as shown in Figures 1 and 2, and described in Section 2.1. This system utilizes software-processing routines to operate scanning algorithms, interpret signals, and enhance sensor response to scatter. Evaluations of various machining parameters and examinations of surfaces, geometric artefacts (edges), defects, and thin film layers in 3D measurements are presented in the following sections, which demonstrate the versatility of this technology.

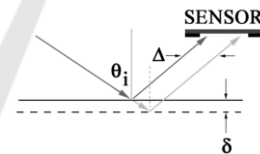


Figure 5a: Optical triangulation geometry.

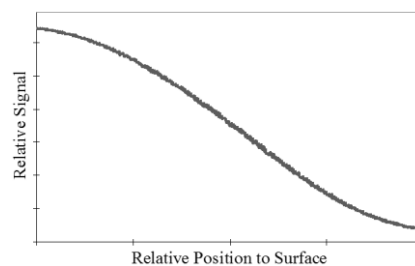


Figure 5b: Response of the sensor-beam arrangement to displacement, δ perpendicular to the surface plane.

2.3.1 Torque Offsets and Thermal Analysis

Ultra-precision machine tools are designed as

integrated systems in gravitationally levelled, vibration isolated, and temperature controlled environments for rotational and translational stability, approaching multi-100 nm error motion. A typical machine tool will operate with pressurized fluid-lubricated bearings supporting the spindle and the track to maintain uniform motion for high accuracy. These tools are provided with operational routines and techniques to match their specifications, and it is beneficial for the operator to periodically measure and monitor performance to maintain repeatable product integrity and yield.

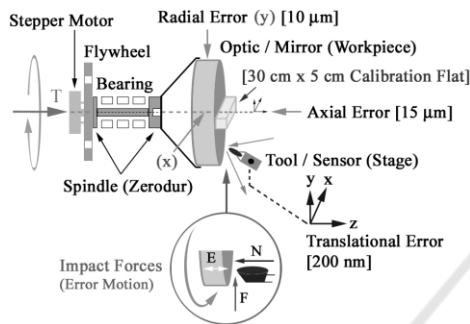


Figure 6: Axial and radial error measurement geometry on the workpiece, and translational error on the cutting tool holder stage. The calibration flat replaces the optic.

The measurement configuration for axial, radial, and translational error motion is shown in Figure 6. A cylindrical work piece is clamped to the spindle in an appropriate manner to ensure rigid coupling, with static preadjustment of its relative position to “true” its surfaces to the spindle and to the tool holder, and thereby reduce error. Typically the front planar surface and the circumferential cylindrical surface are then pre-machined (few μm of removal) to conform workpiece geometry in roundness and planarity to the dynamic circular motion of the spindle and linear motion of the cutting tool, respectively. The cutting tool and the sensor are mounted on a holder stage with translational freedom and nanopositioning capability as required. Mechanical and thermal characteristics of the spindle air-bearing assembly, and translational and rotational accuracy of a precision machine tool were examined in the triangulation-sensing configuration (Figures 5a and 5b) to study the performance of the tool and the sensor. A sensor was placed on axis, parallel to the spindle, which operates free running (100 rpm for approximately 30 min) to stabilize thermally. The vibratory axial error motion on this unit in operation is approximately $\pm 3 \mu\text{m}$ (Figure 7). The rotating spindle exerts paraxial torque, which preferentially repositions the spindle within the

bearing encasement, in an unstable axial position, in the direction of the torque vector.

The spindle rotation was next instantly powered down, and the sharp transition in the data at 3 min. indicates rapid deceleration associated with loss of power, and an axial torque-free realignment of the spindle position within the air bearing encasement. The spindle dynamic-to-static torque offset is $6 \mu\text{m}$ equivalent to the amplitude of the spindle axial error motion. It now commences resting passively, balanced axially and radially within the bearing with uniform air suspension. The bearing temperature was 24.5°C during the rotational phase, cooling off gradually to 22°C , and compressing over tens of minutes, commencing after shut down. The heat from the bearing assembly is gradually transferred to the spindle, which “grows” back to its position during rotation, as the entire spindle-bearing assembly cools and stabilizes in the environment. This thermal growth error is slightly larger than $6 \mu\text{m}$, equivalent to the dynamic axial error, and the torque offset. The ambient air temperature remains steady at 20.7°C during these measurements.

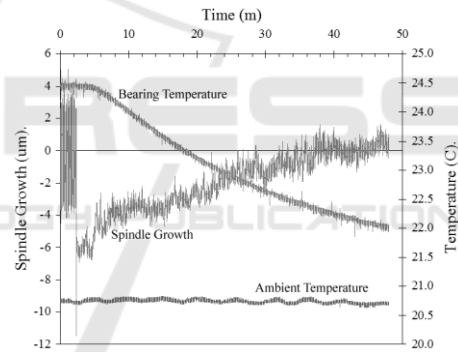


Figure 7: Thermal analysis of a precision spindle.

2.3.2 Cutting Tool Holder-stage Accuracy

The on-axis translational accuracy and hysteresis of the tool stage was evaluated by clamping a commercially available 30 cm x 5 cm polished calibration flat to the spindle chuck (Figure 6), mounting a sensor to the tool holder, and measuring the signal as the sensor tracks the motion of the tool holder in a sequence of 20 steps, 125-nm each, first retracted away from the flat, next 40 steps, 125-nm each, moving toward the flat, and finally 20 steps, 125-nm each, retracted from the flat, back to its original resting position. These results are shown in Figure 8, with a detailed view in the inset. The translational backlash (in the inset) is apparent as progressive motion commands are given to the tool. The overall translational motion is linear with

marginal error of a few 100's nm. With the tool traversing 10- μm total roundtrip translation, from its original resting position, through the 80-step sequence, and returning to it, the total round-trip hysteretic error is under 30 nm.

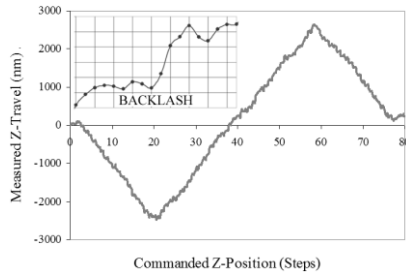


Figure 8: Sensor response to 80x125-nm step pattern. The inset displays the backlash as the tool is advanced.

The translational accuracy of the tool stage, perpendicular to the spindle axis (in the radial direction) was also examined (Figure 9). The sensor in this measurement was first translated across the entire 30-cm length of the calibration flat, then offset 2 μm below the original track, and next translated back to its original position. This data indicates very high repeatability of the tool positioning system with error in the few 100's nm as in the previous on-axis measurements. A fraction of this error contains inaccuracies of the flat and possible contamination of the reflective surface, as is evident in the spurious signals in the first 5 cm measurement range. The flat also appears to have an upward bend beginning at 18 cm, where there is an incremental trend in the data of approximately fewer than 200 nm total. Integrating these measurements, the triaxial x-y-z tool-holder stage motion is shown to be accurate to less than 200 nm with negligible hysteresis.

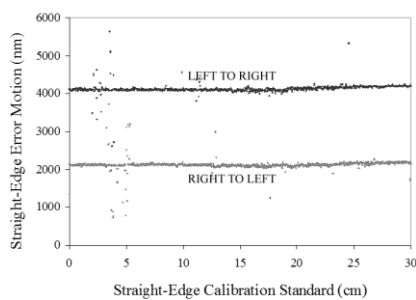


Figure 9: Bi-directional tracking measurements, translating across a 30-cm calibration flat.

2.3.3 Spindle Error Motion

The dynamic axial and radial error motions of a spindle work piece were analysed next, over a 5-

minute period of steady state rotation. The axial measurement data set is shown in Figure 10, evaluated at 100, 500, and 1000 rpm. The 100-rpm axial data has rapid positional fluctuations composed of periodic and aperiodic elements, across the entire measurement duration, in amplitude under 6 μm , combined with gradual axial error variation extending to 15 μm over several minutes. The spindle is observed to settle as the rotational speed is increased to 500 rpm, where the rapid error noise is reduced to less than 1 μm , combined with 15- μm gradual instability over extended time. It stabilizes much further at a speed of 1000 rpm, where the instantaneous positional fluctuation is reduced to less than 500 nm but the long-duration large 15- μm axial variation is persistent in the data. Radial spindle error measurements at 100, 500, and 1000 rpm demonstrate equivalent behaviour, as seen in Figure 11. The radial noise is comprehensively lower than axial noise, which indicates that the spindle as expected is radially more stable within the bearing. The 100-rpm data has rapid periodic and aperiodic fluctuations in the 3- μm amplitude range combined with a slower variation of under 10 μm , extending over duration of several minutes. The stability improves at 500 rpm and the fast error noise reduces to less than 1 μm . The gradual drift is less than 5 μm over the measurement time span, or about 25% of the axial instability. The spindle, rotating at 1000 rpm, registers under a miniscule 250 nm of high frequency noise, with 5 μm of radial instability.

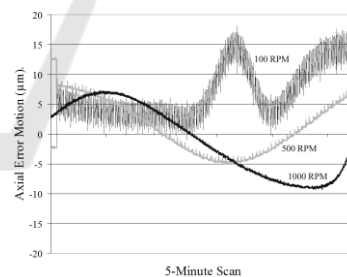


Figure 10: Measurements of axial error motion at 100, 500, and 1000 rpm made over a 5-minute duration.

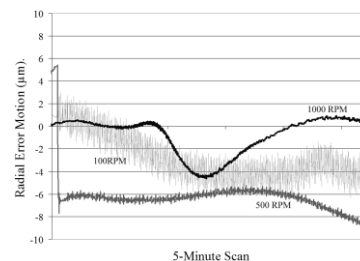


Figure 11: Measurements of radial error motion at 100, 500, and 1000 rpm made over a 5-minute duration.

2.3.4 Ramifications of Spindle Error Noise

The above complement of measurements can be integrated into an overall figure of merit of the precision fabrication capability of this machine tool, to estimate and project the quality of a finished product and manufacturing yield. The limiting factors are as outlined below, focusing on the manner in which spindle error motion produces wear on the cutting tool, which then induces roughness and shape error in the machined surface. The undesirable rotational instabilities in Figures 10 and 11, particularly approaching the 1- μm level and larger (to 15 μm) may be associated with a combination of factors such as torque variations inherent in drive-motor speed inconsistencies and spindle non-uniformities (material, warpage), spindle inertial imbalance, unstable suspension-fluid pressure distribution in the bearing, bearing acoustics, multiple resonances, frictional forces, energy transfer of the spindle to the casing, insufficient machine tool vibration isolation, gravitational level imbalance, thermal gradients and non-uniform heat dissipation, and various other stray factors. An associated factor is that instability at a given point along the inertial axis of the spindle may in reality be smaller in amplitude than the measurement at the workpiece, where it is mechanically levered to a larger amplitude - at a pivot point along the axis within the bearing. Some of these errors can be partially corrected since most precision machine tools do have rebalancing flywheels with passive adjustment to nominally damp non-circular motion; the spindles may also be constructed from low-expansion Zerodur to limit thermal creep. However, a sensor-driven active adjustment and damping system could dynamically reduce the 15- μm slow error to less than 100 nm. Intuitively, the best measurement areas for rotating spindle analysis are on the workpiece, and not directly on the spindle. All of these factors could serve as a case study for future analysis to attain the goal of true nanometre manufacturing.

Referring to Figure 6 (inset), the 15- μm axial and 10- μm radial spindle slow error motions represent equivalent periodic and aperiodic error forces with proportional counter-normal impact (E), originating in torque error (T), and friction (F) transmitted through the workpiece directly to the edge of the cutting tool, which exerts normal force (N) during the machining process; the translational error of the tool-holder stage, and the rapid spindle error motions (100 – 500 nm) are significantly smaller in comparison. These combined forces (E, F, & N)

generate high friction, thermal spikes, and acoustic shock, which produce extremely high localized energy transfer to the cutting tool edge point-of-contact, resulting in wear patterns in the edge profile and its contour, limiting its usable lifetime. The evolution of the edge profile of a cutting tool will be explored in detail in the following section 2.3.5.

Qualitatively, the error noise data indicates that a flat mirror surface, machined utilizing this spindle and a fresh cutting tool, would have radially oriented local roughness texture of depth dimension equal to the axial fluctuations (Figure 10) of the spindle, with relatively smaller contributions from lower radial noise components (Figure 11), which occur in the plane of the surface. The tool positioning error on the order of 100 nm (Figures 8 and 9) is negligible in comparison with the multi- μm level axial and radial fast and slow error noise of the spindle. If the surface is a curved mirror or a lens, machined to a pre-determined contour, the dynamic axial and radial error-motion could result in proportional roughness and shape variations caused by the instability of the spindle. The axial error would induce radially oriented roughness in the finished surface, while the radial error could modulate this roughness texture. These two error factors would combine and contribute localized geometric modulations to the shape of the surface as the contour is machined. As with any large mechanically driven periodic system at low-rpm operation, the axial and radial data exhibit considerable inertial imbalance and potential low frequency resonances in the tool. These instabilities are damped at much higher rotational rates, producing a relatively smooth cutting operation. The machining of precision mirrors, lenses, and flats requires careful consideration of multiple factors, and evaluation of tool performance at various speeds to determine the most suitable operational parameters for the highest quality optical products.

This complement of measurements and analysis has additional applications: it can be utilized for evaluating and optimising spindle and stage design, implementing motion stability, damping resonances, streamlining bearings, improving vibration isolation, and reducing thermal gradients – all important factors in the design and manufacture of nanometre precision machine tools. It can also be utilized to determine the optimal operating points for spindle rotation, bearing fluid pressure, cutting tool depth and feed, coolant flow, temperature, and machine tool stability, and thus shorten the decision making process leading to nanometre surface and shape quality with high yield.

2.3.5 Diamond Cutting Tool Edge Profile

The next measurement in our evaluation sequence is the cutting tool profile, and the progression of wear during the machining operation. We focus particularly on precision single-point diamond turning (SPDT), utilizing commercially available diamond cutting tools, for the fabrication of precision mirrors and optics. These tools are specified in terms of their contour (nose) radius, cutting point transverse edge radius, edge roughness, edge roundness, edge straightness, cutter angle, and rake angle. The primary measurement of interest in SPDT is the edge contour, as related to the nose radius, since edge wear is directly correlated to finished surface quality. Among various tool parameters, contour wear is a good figure of merit, and is directly dependent on usage duration, cutting depth, spindle and stage error motions, thermal gradients originating in frictional forces in the cutting process, machining parameters such as rotational speed and feed rate, surface material properties, and the quality of the diamond crystal. Edge contours on diamond tools were examined, one freshly manufactured and another measured after its utilization to form multiple lenses. The two tools had zero rake angles, edge radius on the order of $< 2 \mu\text{m}$, 60-degree cutter angle, and contour radius of 0.2 mm. These diamond tools are fabricated by polishing with progressively finer diamond particles in controlled processes. They may contain intrinsic crystalline defects and sub-surface damage induced during fabrication.

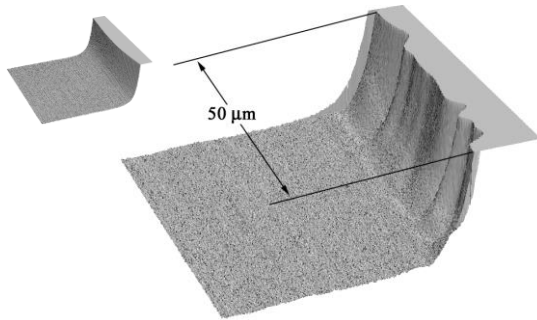


Figure 12: Contour of a used diamond tool showing wear grooves across the edge. The inset is a fresh tool.

The fresh tool was measured at the cutting point, and the data shown in Figure 12 (inset) indicates pristine edge quality, and smooth rake. The local radius conforms to the manufacturer specification of 0.2 mm with minimal edge roughness and no visible edge defects. The edge straightness also appears to

be uniform, without any manufacturing artefacts such as polishing striations across the edge. The tool utilized in manufacturing optical lenses has multiple features of interest, resulting from wear, including a modulated edge-contour profile descending into deep furrows which span from the rake face downwards, into the base. The regions of modulation, have dimensions of a few to $10 \mu\text{m}$, superimposed on the original edge. The multi- μm waviness of the edge contour indicates that spindle error motion (which is of equivalent multi- μm oscillation) is a major contributing factor in this degradation. In SPDT, the error motion induces equivalent periodic high impact forces on the cutting tool edge within its microscopic area of contact with the surface, typically on the order of $2\text{-}\mu\text{m}$ (width) \times $10\text{-}\mu\text{m}$ (cutting arc) or less (Figure 6, inset). These error-noise forces in combination with frictional forces, acoustic shock, and thermal gradients during machining perturb and damage the cutting tool edge at its points of weakness: defect sites, its polish roughness structure, and its subsurface damage. The wear regions along the contour appear to have become progressively deeper with usage, rendering the cutting edge unusable. This cutting tool will inevitably leave these imprints on the machined surface, resulting in a poor quality product with noticeable optical imperfections and local shape irregularities. In combination with all of the measurements and discussion in Section 2.3.4 the overall quality of a machined surface utilizing this cutting tool, at low rpm, would not result in optical quality surfaces and shapes.

2.3.6 Surface, Defect, and Thin Film Data

Optical scatter is routinely utilized to examine smooth surfaces and to identify defects in the optics and the semiconductor industries, including thin films, and multi-layer and photoresist-patterned substrates. The geometrical arrangement to perform these functions is shown in Figure 1. A detector is positioned to the surface, oriented to capture scatter radiation in a solid angle, defined by the angle of incidence and the polarization of the input beam. Since non-specular scatter is typically of low intensity for smooth surfaces, the detector is coupled to low noise, high gain electronics, and may also include capability to select a particular polarization to enhance feature-to-background sensitivity. The nanometre scanning stage combined with software processing can produce contrast-enhanced images of surface structure and roughness, defects, and sub-surface damage. Figure 13 shows the scatter image

of a diamond-turned Si surface in a $50\mu\text{m} \times 50\mu\text{m}$ field. In the machining process, the spindle operated at 1000 rpm, and a 1.5-mm diamond tool was advanced in $3\text{-}\mu\text{m}$ steps/rev, with $1.3\text{-}\mu\text{m}$ removal, and impressed corresponding indentations on the Si surface in a regular pattern; the total surface area of the Si-wafer section was 1 cm^2 and the tool edge profile was unknown. The surface is linear along the y-axis but has large irregular shape inaccuracy, on the order of $10 - 25\ \mu\text{m}$, along the x-axis, perpendicular to the grating, equivalent to and perhaps caused by error motion as the cutting tool traverses the surface (See discussion in Section 2.3.4). This data indicates that if a large optic or mirror was manufactured utilizing this machine and cutting tool combination, μm -scale surface and shape irregularities would undoubtedly occur in the finished product. In general, to quantify similar surface errors, the cutting tool and a sensor could be mounted on identical arcuate positions on the holder (Figure 6). It would then be possible to first cut the surface, and then measure its contour to determine its accuracy within limits of the error noise of the machine tool.

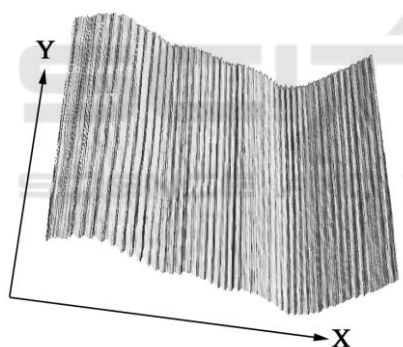


Figure 13: $50\mu\text{m} \times 50\mu\text{m}$ scatter image of diamond-turned Si showing local cutting tool indentations and overall shape error.

Perfectly smooth planar polished surfaces were also measured but displayed no interesting features related to microstructure and defects, beyond a simple flat field in the data indicating that the entire scatter profile was confined to the specular region with minimal Lambertian haze and no detectable offset scatter components. This data was verified by AFM measurements and analysis in the identical vicinity of the surface.

We progress to examining the scatter features of a defect. A commercially available polished quartz blank was scanned with the same parametric

settings, and the data is shown in Figure 14. The data contains several observable features: low frequency wave-like roughness oriented perpendicular to the x-axis of spatial period about $10\ \mu\text{m}$ in the foreground. Towards the rear of the sample the structure appears to be two-dimensional, oriented randomly along both axes of $5\text{-}10\ \mu\text{m}$ dimensions, and includes peripheral geometry of a second defect in the far corner. The defect pit (identified in the semiconductor industry as a crystal originated pit or COP; see inset AFM image) in the centre is approximately $15\ \mu\text{m}$ in diameter, and produces scatter, which indicates the presence of some shallow vertical projections in the range of a few micrometers forming concentric rings. The inner ring has wavelike rim structure, while the surrounding ring appears somewhat regular and shallow. The defect also appears to have an internal bridge, spanning the pit bisecting it parallel to the y-axis.

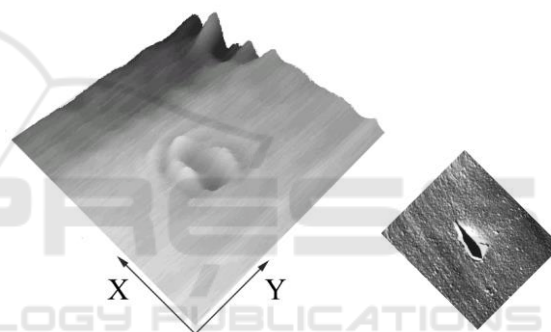


Figure 14: Defect on quartz surface ($50\mu\text{m} \times 50\mu\text{m}$)(L). The surface structure appears to be composed of wave like patterns with particular orientation. AFM image of a similar defect and surface structure on the same sample is shown (R).

In a final measurement, a composite 200-nm (50-nm Cr and 150-nm Au), $75\ \mu\text{m} \times 75\ \mu\text{m}$ thin film pad, deposited by e-beam evaporation on a Si wafer, was imaged to examine the scatter produced by the structure of the film, the edges, and the corner. The data is shown in Figure 15 and reveals compositional information about the film, in greater detail than could be observable by diffraction-limited high-resolution optical microscopy. The 200-nm total film thickness is identifiable, as indicated on the data, despite scaling to approximately only 25% of the wavelength of optical beam, and indicating very good depth sensitivity of the scatterometer-triangulation technique. The darker base region of the film is very likely low-reflectivity Cr material, while the brighter scatter data in the upper region is associated with

highly reflective Au. The surface of the film appears to have randomly oriented two-dimensional fine grain structure in the spatial frequency range of a few micrometers laterally but extending only a few 10's of nanometres in roughness vertically, remarkably just under 3% in dimensional comparison with the sensing wavelength. These appear to be islands of molecular nucleation forming crystallite fractals of the Au material, generated progressively as the film is deposited. Some of this structure may also include the underlying structure of the Cr film.

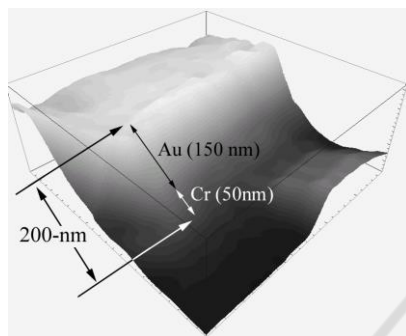


Figure 15: 200-nm Cr-Au film on Si. The film thickness is as shown, and the surface of the film appears to indicate structure formed by nucleation.

There is a uniform ridge along the upper peripheral edges of the film, related to the photoresist-mask pattern utilized in the lithographic lift-off fabrication process. Similar dielectric and metal thin films are routinely deposited on optics (anti-reflection coatings) and semiconductor wafers (device connections and contacts), whose structure and function could be examined by this technique.

3 CONCLUSIONS

Laser triangulation combined with detection by a sub-nanometre resolution sensor is presented as a versatile, contact-free, non-invasive method to monitor and evaluate ultra-precision machine tool operation, and to examine the surface and shape quality of μm -size to meter-size optical and semiconductor products to accuracy of less than 200 nm, and potentially approaching 10 nm. The thermal stability, axial torque displacement, spindle “growth”, tool holder stage error and hysteresis, and the axial and radial error motion of a precision machine tool spindle were resolved with this apparatus in the range of < 100 nm to several μm . A diamond cutting tool edge had 10- μm wear patterns,

which developed after multiple usage cycles, originating in spindle error motion. An SPDT Si surface was shown to have indented lines equivalent to the machining settings, with large overall 10 - 25 μm shape variations. This set of measurements and analysis could be utilized to design nanometre precision machine tools, optimise critical components like the spindle and the bearing, facilitate vibration isolation, and select operating parameters to fabricate products with high quality and large yield. Textured surface structure with defects and internal defect structure were identified on a quartz optical flat. Finally, a thin Cr-Au film was examined, and the 200-nm thickness of the film is easily identifiable together with approximately 20-nm fractal nucleation structure on the surface of the film. We have demonstrated the versatility, adaptability, and reliability of this technology for use in the manufacture of optical, semiconductor, and other industrial products manufactured from a multitude of materials, regardless of size.

ACKNOWLEDGEMENTS

Financial and/or technical assistance for this work was provided from several sources at various times, including the US Naval Research Laboratory, California Institute of Technology, US Air Force, NASA – Jet Propulsion Laboratory, the Livermore Laboratory, the National Research Council, and E.F. and B.F. Soares.

REFERENCES

- Azzam, R., and Bashara, N., 1999. *Ellipsometry and Polarized Light*, Elsevier.
- Heavens, O., 1955. *Optical Properties of Thin Solid Films*, Dover.
- Church, E., Jenkinson, H., and Zavada, J., 1979. *Relationship between Surface Scattering and Microtopographic Features*, *Optical Engineering* 18 (2).
- Longuet-Higgins, M., 1957. Statistical Properties of an Isotropic Random Surface, *Phil. Trans. A*, 250.
- Stover, J., 1995. *Optical Scattering*, *SPIE Optical Engineering Press*, Washington, 2nd edition.
- Bohren, C., and Huffman, D., 1998. *Absorption and Scattering of Light by Small Particles*, John Wiley.
- Sze, S., 1981. *Physics of Semiconductor Devices*, John Wiley, 2nd edition.
- Horowitz, P., and Hill, W., 1989. *The Art of Electronics*, Cambridge University Press, 2nd edition.